

# Journal of Materials Chemistry A

Accepted Manuscript



This is an *Accepted Manuscript*, which has been through the Royal Society of Chemistry peer review process and has been accepted for publication.

*Accepted Manuscripts* are published online shortly after acceptance, before technical editing, formatting and proof reading. Using this free service, authors can make their results available to the community, in citable form, before we publish the edited article. We will replace this *Accepted Manuscript* with the edited and formatted *Advance Article* as soon as it is available.

You can find more information about *Accepted Manuscripts* in the [Information for Authors](#).

Please note that technical editing may introduce minor changes to the text and/or graphics, which may alter content. The journal's standard [Terms & Conditions](#) and the [Ethical guidelines](#) still apply. In no event shall the Royal Society of Chemistry be held responsible for any errors or omissions in this *Accepted Manuscript* or any consequences arising from the use of any information it contains.

# Magnetic Particles-based Super-Hydrophobic Coatings with Excellent Anti-icing and Thermo-responsive Deicing Performances

Tiantian cheng, Ren He, Qinghua Zhang\*, Xiaoli Zhan, Fengqiu Chen

College of Chemical and Biochemical Engineering, Zhejiang University, Hangzhou 310027, China

Magnetic nanoparticles (MNP) were introduced as the heat mediator in the superhydrophobic coating for anti-icing and deicing performance in this article. The fluorinated copolymer tethered epoxy groups was synthesized and mixed with amino modified  $\text{Fe}_3\text{O}_4$  nanoparticles, and then crosslinked with diethylenetriamine to obtain novel multifunctional magnetic hybrid coatings. The compositions, morphologies, surface microstructure and wettability performance of the hybrid coatings were systematically investigated by the scanning electron microscopy (SEM), atomic force microscopy (AFM), X-ray photoelectron spectroscopy (XPS), and water contact angle (WCA) measurements. The target coatings exhibited excellent superhydrophobicity and wetting stability driven from the formation of micro-nano hierarchical surface roughness covered with fluorinated groups. The low temperature ( $-15\text{ }^\circ\text{C}$ , RH  $50 \pm 5\%$ ) WCA showed that the superhydrophobic surface could delay the freezing time from 50 s to 2878 s. And the ice adhesion strength was significantly lower than that of pure copolymer coating. More importantly, the outstanding photothermy and magnetothermal effect of the magnetic particles imparted the coatings with long time icing delay and thermal de-icing property. The fabricated multifunctional superhydrophobic surfaces with excellent anti-icing and active deicing properties will be promising for practical application.

## 1. Introduction

Superhydrophobic surfaces (SHS) with high contact angle (CA) and a low water adhesion have received tremendous scientific interest recently.<sup>1,2</sup> Inspired by the "lotus effect", a number of SHS with special wettability have been developed.<sup>3-5</sup> These surfaces promise a wide range of potential applications in marine coating,<sup>6</sup> oil/water separation,<sup>7</sup> and anti-icing,<sup>8</sup> due to the smart and self-cleaning<sup>9,10</sup> ability of the surface. Using the SHS to prevent freezing process has been a hot topic in recent years. The anti-icing properties of SHS may be attributed to three reasons. One is the easily removal of overcooled water droplets before they freeze.<sup>11</sup> The other is the delay of crystallization<sup>12</sup> caused by lower freezing point<sup>13</sup> or increasing barrier for heat transfer<sup>14</sup>. The third reason is that ice

---

\* Corresponding author at: College of Chemical and Biochemical Engineering, Zhejiang University, Hangzhou 310027, China. Fax: +86 571 87991227. E-mail address: qhzhang@zju.edu.cn (QH. Zhang).

† Electronic supplementary information (ESI) available: Movies showing the water droplets roll-off from the superhydrophobic surface; Size distribution of  $\text{MNP@NH}_2$ , three dimensional AFM phase images of MNP-50, and the composition of the four samples. See DOI: 10.1039/x0xx00000x

adhesion is weakened when ice is accumulated on the surface.<sup>15</sup> We have reported that it takes some minutes or even hours for water to be frozen on the SHS under overcooled environment due to SHS can trap air in multiscale rough surface textures.<sup>16-18</sup>

It is widely accepted that low surface energies and high surface roughness values are required to fabricate SHS.<sup>1,19,20</sup> A lot of efforts have been devoted to prepare superhydrophobic surface and optimize its structure to improve the water repellency and anti-icing properties.<sup>21</sup> Significantly delayed ice formation and reduced ice adhesion or accumulations have been reported for various SHS.<sup>22</sup> Theoretical models were also developed to demonstrate how SHS could delay ice formation from impinging water droplets, which was in good agreement with experimental work.<sup>14,23</sup>

At the same time, some researchers have raised doubts about SHS as high efficient anti-icing materials with durable service under different conditions.<sup>24</sup> Some SHS were reported to lose anti-icing properties in a humid atmosphere,<sup>25</sup> if icing followed water condensation or frost formation in their rough structures.<sup>26,27</sup> These SHS shifted from Cassie to Wenzel wetting states under low temperature and high relative humidity.<sup>28</sup> Several types of SHS with relatively poor performance were reported under repeated icing/deicing cycles,<sup>29</sup> which was attributed to their poor abrasive resistance and stability. The designed rough structure may even be damaged by volume expansion in ice formation process.<sup>30</sup> Once ice forms on SHS, the ice adhesion strength would be enlarged when ice penetrates into the surface texture. The traditional ways to remove ice include manual deicing and mechanical deicing method. However, these methods involve problems such as time consuming, low efficiency, and equipment wear.<sup>31</sup>

It is an effective anti-icing method to keep the surface temperature thermally above the freezing point under icing conditions.<sup>31</sup> Especially for deicing properties of transmission lines, utilization of the Joule effect for heating line conductors is recognized as the most efficient engineering approach worldwide.<sup>32</sup> This deicing method, however, is high cost and energy consumption.<sup>33</sup> Magnetic nanomaterials were also reported to be used as mediators of heat because of their intrinsic ability to absorb energy from light<sup>34,35</sup> and be heated under external ac magnetic fields<sup>36,37</sup>. Nanocomposite magnetic materials have attracted much attention due to their novel physical properties such as electrical conductivity, sensitivity towards magnetic fields, and light absorption potential.<sup>38,39</sup> Magnetic Fe<sub>3</sub>O<sub>4</sub> nanoparticles are usually dispersed in a polymeric phase to prepare magnetic nanocomposites with both magnetic properties and mechanical strength. Compared to blending, the covalent integration of the particulate component can enhance the structural function of composite materials.<sup>40</sup> It is known that fabrication of superhydrophobic surfaces could drive from the bio-inspired surfaces with micro-nanostructures and low surface energy groups.<sup>41</sup> SHS can be prepared by incorporation of Fe<sub>3</sub>O<sub>4</sub> nanoparticles into fluorinated copolymers with low surface energy.<sup>42</sup> This multifunctional surface would combine active deicing via photothermal and magnetothermal effect with passive anti-icing via superhydrophobic performance.

It is confirmed that the superhydrophobic coatings composed of nano-micro roughness structure and low surface energy groups have a good application foreground in anti-icing performance.<sup>19,43</sup> The pioneering work is encouraging but still has some problems, *e.g.*, high cost and difficult recycling.

Once these superhydrophobic roughness surfaces were iced or frosted under extreme conditions, it's a challenge to deicing effectively by artificial method. To overcome this problem, we attempted to fabricate multifunctional superhydrophobic surfaces with excellent anti-icing property and active deicing potential. In this study, the amino-functionalized magnetite particles (MNP@NH<sub>2</sub>) were prepared by treating Fe<sub>3</sub>O<sub>4</sub> with  $\gamma$ -aminopropyltriethoxysilane to improve the dispersing and reactivity. The fluorinated copolymer modified with epoxy groups was synthesized by free radical polymerization. Then the magnetic hybrid coating with the covalent integration was prepared by crosslinking fluorinated copolymer, MNP@NH<sub>2</sub>, and polyamine compound. The wettability of the hybrid materials associated with surface roughness and chemical composition were discussed. The superhydrophobic performance and the anti-icing properties of the magnetic hybrid surfaces were explored. Glaze ice was prepared by spraying water micro-droplets at subzero temperature, i.e. under conditions very close to outdoor ice accretion. The magnetism property, thermomagnetic, and photothermal effect of these magnetic hybrid coatings were investigated. Furthermore, the icing/ice-melting cycle process by photothermal effect was applied to evaluate the anti-icing durability of the coatings.

## 2. Experimental section

### 2.1 Materials

Iron (II) chloride tetrahydrate (FeCl<sub>2</sub>·4H<sub>2</sub>O, 99% purity), diethylenetriamine, and glycidyl methacrylate (GMA) were purchased from Aldrich. [N-methyl-perfluorohexane-1-sulfonamide] ethyl (meth)acrylate (C<sub>6</sub>SMA) was synthesized as described in our previous work.<sup>44</sup> Stearyl methylacrylate (SMA) was provided by Juhua Group Corporation. 2,2'-azobisisobutyronitrile (AIBN, Aldrich) was recrystallized from ethanol.  $\gamma$ -aminopropyltriethoxysilane (APTES, purity>98%), Iron (III) chloride anhydrous (FeCl<sub>3</sub>, cp), ammonia (NH<sub>4</sub>OH, 25~28% v/v aqueous), and hydrazine hydrate (N<sub>2</sub>H<sub>4</sub>·H<sub>2</sub>O, 85 wt%) were purchased from Sinopharm Chemical Regent Co., Ltd. Other reagents and organic solvents, unless specific illumination, were purchased from Sinopharm Chemical Regent Co., Ltd. and used without any further purification.

### 2.2 Sample preparation

**2.2.1 Synthesis of amino functionalized Fe<sub>3</sub>O<sub>4</sub> particles** Fe<sub>3</sub>O<sub>4</sub> was prepared according to the previous report.<sup>45,46</sup> Deionized water (100 mL), N<sub>2</sub>H<sub>4</sub>·H<sub>2</sub>O (1.0 g), FeCl<sub>2</sub>·4H<sub>2</sub>O (9.95 g), and FeCl<sub>3</sub> (14.22 g) were added to a three-necked round bottom flask equipped with a mechanical stirrer. After the mixture was agitated for 30 min to eliminate oxygen, NH<sub>4</sub>OH (30 mL) and deionized water (10 mL) were quickly syringed into the flask with vigorous stirring. Then the Fe<sub>3</sub>O<sub>4</sub> particles were magnetically separated from the supernatant and were redispersed in distilled water for at least three times until pH=7, washed thoroughly with ethanol, collected by an external permanent magnet, and noted as MNP. The obtained MNPs were further functionalized by amino and the process is as follows. MNP (3 g) and APTES (5 mL) were dispersed into ethanol (80 mL) with nitrogen protection. After the mixture was mechanically stirred for 10 h at 60 °C, the crude APTES-coated MNP particles were obtained.

They were washed thoroughly with ethanol and collected by an external permanent magnet to get the amino functionalized MNP particles (noted as MNP@NH<sub>2</sub>).

**2.2.2 Synthesis of copolymer P(C<sub>6</sub>SMA-r-SMA-r-GMA)** The fluorinated copolymer P(C<sub>6</sub>SMA-r-SMA-r-GMA) was prepared by solvent polymerization. A typical copolymerization process was as following. C<sub>6</sub>SMA (2.86 mmol), SMA (11.08 mmol), and GMA (1.76 mmol) were dissolved in butyl acetate (15 mL) with nitrogen protection. Then AIBN (0.10 g) as initiator was added into the reactor at 80 °C. After 10 h of polymerization, the crude copolymer was precipitated in methanol, dried in a vacuum oven, redissolved in tetrahydrofuran (THF), precipitated from THF solution with excess methanol, and finally dried by vacuum oven at 50 °C.

**2.2.3 Preparation of MNP@NH<sub>2</sub>@P(C<sub>6</sub>SMA-r-SMA-r-GMA) composite coating** In this step, the P(C<sub>6</sub>SMA-r-SMA-r-GMA) dissolved in butyl acetate was mixed with diethylenetriamine by ultrasonic for 20 min, then the MNP@NH<sub>2</sub> solution in n-butyl acetate was added and ultrasonicated for another 10 min. The obtained mixture was sprayed onto glasses or silicon. MNP@NH<sub>2</sub>@P(C<sub>6</sub>SMA-r-SMA-r-GMA) composite films (noted as hybrid coating) were allowed to cure for 2 h at room temperature, followed by an additional 12 h vacuum drying in an oven at 150 °C. Four film samples were prepared in this work. The contents of MNP@NH<sub>2</sub> for these four samples are 0, 10 wt%, 30 wt%, and 50 wt%, respectively. The detailed compositions of the hybrid coatings are listed in ESI Table s1 †.

## 2.3 Characterizations

**2.3.1 Chemical structure and composition** FTIR spectra were performed on Nicolet 5700 FT-IR to determine the structure of samples using KBr pellet method. The chemical composition of the coating was analyzed by XPS (Thermo Scientific, USA) with an Al K $\alpha$  X-ray source. The X-ray gun was operated at 14 kV and 350 mW, and the analyzer chamber pressure was 10<sup>-9</sup>-10<sup>-10</sup> Pa. Dynamic light scattering (DLS) measurements were performed at 20 °C on laser particle size analyzer (LS-230 Coulter).

**2.3.2 Surface topography** The surface morphologies of the final surfaces were examined by SEM analysis (SIRISON, FEI) and AFM (Veeco, USA). AFM was operated in tapping mode. The scanning range was 5  $\mu$ m  $\times$  5  $\mu$ m. The root-mean-square (RMS) roughness value was calculated from the obtained image.

**2.3.3 Magnetic property and magnetothermal effects** Magnetic studies of samples were carried out on a TOEI VSM-5 vibrating sample magnetometer (VSM) at 293 K. A high frequency induction heater (manufacturer: double-Power Technology Co., Ltd., Shenzhen; Model: SP-35AB 35 kW) was employed for magnetothermal experiments.

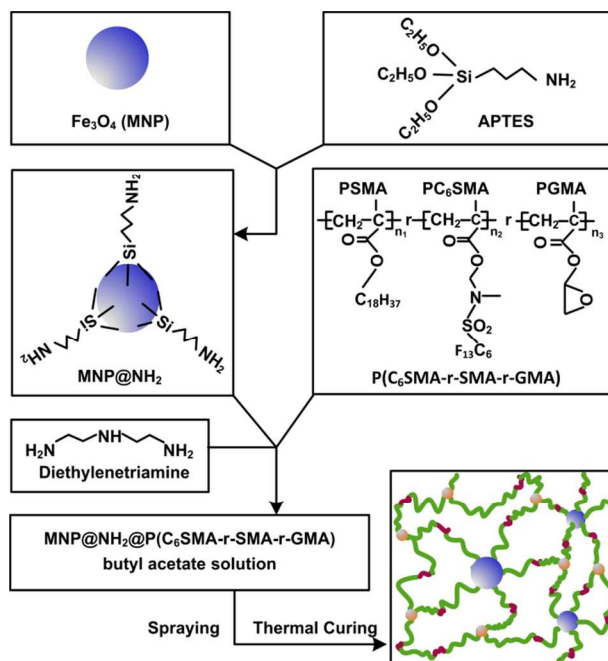
**2.3.4 Anti-icing properties** Contact angles (CA) measurements were performed on CAM 200 optical contact-angle goniometer (KSV Instruments, Helsinki, Finland) at both the ambient temperature and cold condition. Then the advanced angles and receding angles can be calculated from the measured results. The volume of the tested water droplet is 2  $\mu$ L. The sliding angles of the drops were measured by tilting the sample stage from zero to higher angle until the droplet rolled off the surface

at room temperature and were recorded by the optical CCD of the system. Icing delay time (DT) of water droplets on superhydrophobic surfaces was tested in situ by the high speed CCD camera. It was performed by controlling the room temperature down to  $-15\text{ }^{\circ}\text{C}$  on a Peltier cooling controller with a control precision of  $0.5\text{ }^{\circ}\text{C}$ . During the measuring process, the water drops changed from transparent to non-transparent, indicating the water was frozen. The delay time (DT) was defined as the time that the droplet changed from transparent to non-transparent. The room temperature was  $23 \pm 2\text{ }^{\circ}\text{C}$  and the relative humidity was  $50 \pm 5\%$  controlled by a humidifier. The ice adhesion strength was measured by the method as described in literature.<sup>47</sup> This adhesion was considered to be the shear strength needed to remove the ice from the coating. Bottomless cuvettes were placed again onto the coating and were filled with the liquid water, which were kept at  $-15\text{ }^{\circ}\text{C}$  for another 5 hours to form the ice. Compressed air with a certain intensity of pressure was used to blow ice. The pressure of the condensed air increased at a rate of  $6.8\text{ KPa}/(3\text{ s})$  until the ice was sheared off, which was recorded as the ice adhesion strength.

**2.3.6 De-icing properties** The de-icing properties of coatings, absorbing energy from the sunlight, were tested by recording the melting time of ice on the surface with the rise of temperature. Glaze ice was prepared by spraying water micro-droplets (mimic freezing rain) onto the as-prepared samples at subzero temperature, i.e.  $<-10\text{ }^{\circ}\text{C}$  and  $\text{RH} \approx 80\%$ . All samples were kept in the mimic freezing rain environment for 4 h. And then, these surfaces with ice accretion were further to be frozen under  $-15\text{ }^{\circ}\text{C}$  and  $\text{RH} \approx 70\%$  conditions, mimicking the formation of glaze. The photothermal deicing tests were investigated in  $<-5\text{ }^{\circ}\text{C}$  and  $\text{RH} \approx 70\%$  environment, where the as-prepared samples were exposed to a sunlamp light (75 W). The rise of temperature was controlled by a sunlamp (75 W), which was used as the solar simulator source. The temperature was measured by a MT4 MAX infrared thermometer from Fluke Co., USA. The distance between the sunlamp and the coating surfaces was 50 cm.

### 3. Results and discussion

Scheme 1 illustrates the typical fabricating procedures of the hybrid coatings. The  $\text{MNP@NH}_2\text{@P}(\text{C}_6\text{SMA-r-SMA-r-GMA})$  hybrid coatings were prepared via a simple crosslinking process by mixing  $\text{P}(\text{C}_6\text{SMA-r-SMA-r-GMA})$ , diethylenetriamine, and  $\text{MNP@NH}_2$ . During the process, MNP with organic reactive groups on the surfaces were dispersed uniformly in the mixture solution. The fluorinated copolymers of  $\text{P}(\text{C}_6\text{SMA-r-SMA-r-GMA})$  that contain epoxy groups could react with diethylenetriamine and  $\text{MNP@NH}_2$  both of which contain amino groups. As a result, MNP covered with the epoxy resin network were formed with low surface energy fluorinated chains. The  $\text{MNP@NH}_2\text{@P}(\text{C}_6\text{SMA-r-SMA-r-GMA})$  in butyl acetate solution was then sprayed on substrates, followed by heat treatments which promoted the crosslinking and enrichment of fluorocarbon chains onto the coating surface. Therefore, the hybrid coatings with the covalent integration were obtained.



Scheme 1. Synthesis route of  $\text{MNP}@NH_2@P(\text{C}_6\text{SMA}-r\text{-SMA}-r\text{-GMA})$  coating.

### 3.1 Structure characterization

The chemical structures of synthesized MNP,  $\text{MNP}@NH_2$ , fluorinated copolymer ( $\text{P}(\text{C}_6\text{SMA}-r\text{-SMA}-r\text{-GMA})$ ), MNP-0, MNP-10, MNP-30, and MNP-50 were identified by FT-IR spectra described in Fig. 1. The adsorption peak at around  $580\text{ cm}^{-1}$  was assigned to Fe-O group of MNP, which confirmed the presence of magnetite nanoparticles. The signals of Fe-O-Si bonds for  $\text{MNP}@NH_2$  appeared at around  $584\text{ cm}^{-1}$  overlap with the Fe-O vibrations.<sup>48</sup> The bands at  $1124$  and  $1046\text{ cm}^{-1}$  were corresponding to the Si-O-H and Si-O-Si groups, respectively. The other two broad bands at  $3380$  and  $1629\text{ cm}^{-1}$  were ascribed to the N-H and  $\text{NH}_2$  stretching vibration. Therefore, the FTIR spectra of MNP and  $\text{MNP}@NH_2$  indicate that the amino silane have been grafted on the surface of magnetite particles. For the copolymer, peaks at  $913\text{ cm}^{-1}$  were corresponding to symmetric stretching of epoxy group. The characteristic absorptions of C-F ( $1050\text{-}1300\text{ cm}^{-1}$ ) and C=O ( $1735\text{ cm}^{-1}$ ) were clearly visible. The results suggest that fluorinated copolymer containing epoxy groups was successfully synthesized. For MNP-0, MNP-10, MNP-30, and MNP-50 samples, the broad bands around  $3437\text{ cm}^{-1}$  were assigned to -NH- and -OH groups. With more  $\text{MNP}@NH_2$  added, the intensity of C-H vibrations from  $\text{CH}_2$  asymmetric and symmetric stretching at  $2926$  and  $2854\text{ cm}^{-1}$  decreased, while the Fe-O vibrations at  $580\text{ cm}^{-1}$  increased. The peaks at  $913\text{ cm}^{-1}$  corresponding to epoxy groups were not observed for these four samples, indicating the complete reaction among the fluorinated copolymer, amino curing agent, and  $\text{MNP}@NH_2$ .

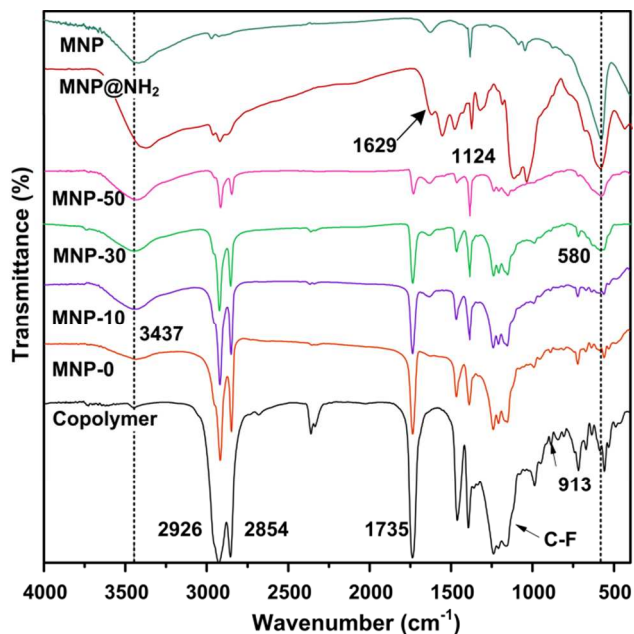
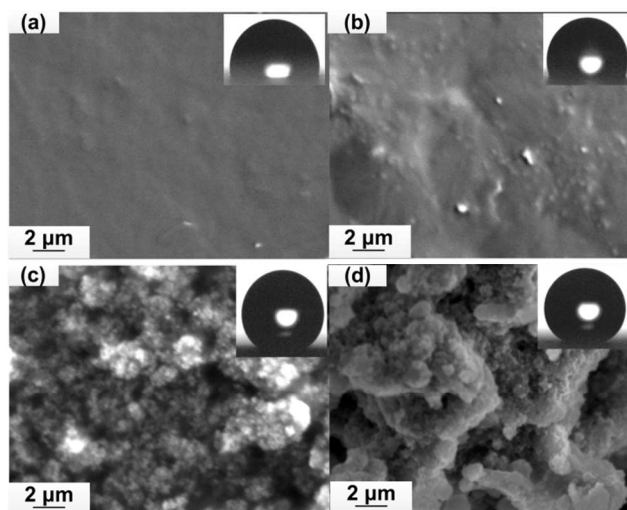


Fig. 1 FT-IR spectra of MNP, MNP@NH<sub>2</sub>, Copolymer, MNP-0, MNP-10, MNP-30, and MNP-50.

### 3.2 Surface topography

The size distributions of the prepared MNP@NH<sub>2</sub> were obtained from DLS measurement (shown in ESI Fig. s1 †), indicating the presence of small clusters consisting of nanoparticles. To study the surface topography and roughness structure of the hybrid coatings, SEM and AFM techniques were used. Fig. 2 shows SEM images of the hybrid coatings containing MNP@NH<sub>2</sub> from 0 wt% to 50 wt%. The pure copolymer coating MNP-0 had smooth network structure (Fig. 2a), while obvious protuberances appeared for MNP-10 in nanoscale (Fig. 2b). And for MNP-30 and MNP-50 (shown in Fig. 2c, d, and ESI Fig. s2 †), the agglomerated micro apophyses composed of nanoparticles could be seen. As the amounts of MNP@NH<sub>2</sub> increased to 30 wt% and 50 wt%, the aggregation structures with micro-nanocomposite roughness were formed on the coatings. Therefore, the hybrid coatings with hierarchical structure were obtained.

Tapping mode atomic force microscopy (AFM) was applied to further investigate the surface structure of the hybrid coatings. In case of three dimensional height images of AFM (Fig. 3), the RMS values of MNP-0, MNP-10, MNP-30, and MNP-50 were 7.16 nm, 26.67 nm, 109.97 nm, and 146.92 nm, respectively. Irregular nanoparticle clusters were obviously visible on the micro apophyses in Fig. 3c, and d. The presences of hierarchical multi-scale surface roughness for the samples with high MNP contents were evidenced by SEM and AFM characterizations. The spacing between the textural peaks of roughness was vital to trap air in the pockets. Hence for the prepared hybrid material, the water droplet cannot penetrate into the pitch profile, which results in a high static contact angle and low adhesion.



**Fig. 2** SEM images of MNP-0 (a), MNP-10 (b), MNP-30 (c), and MNP-50 (d). Contact angles appear in inserts.

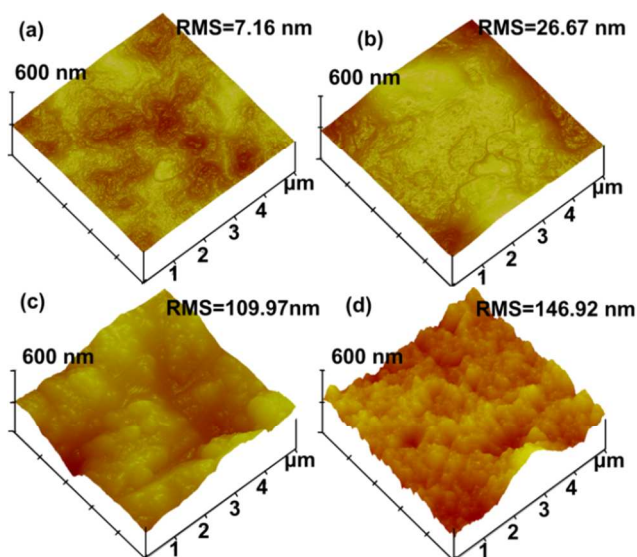


**Fig.3** The typical three dimensional AFM height images of MNP-0 (a), MNP-10 (b), MNP-30 (c), and MNP-50 (d)

### 3.3 Surface elemental compositions

The quantitative elemental compositions ( $C_{1s}$ ,  $O_{1s}$ , and  $F_{1s}$ ) of the hybrid coatings could be evaluated from XPS results. Fig. 4 displays the high resolution XPS spectra of the fluorinated nanocomposite coatings with different contents of MNP@NH<sub>2</sub>. As shown in Fig. 4, the high binding energy of 685.5 eV was attributed to the F element in the P(C<sub>6</sub>SMA-r-SMA-r-GMA). For both samples, the fluorine atomic ratio on the surfaces was obviously higher than that of the bulk. This is because the fluorinated groups significantly enrich on the surface, which can impart the coating with very low surface energy. This phenomenon indicated that the superhydrophobic surface in Cassie state can be

achieved by fabricating micro-nano hierarchical structured films modified with hydrophobic organic groups at ambient temperature.

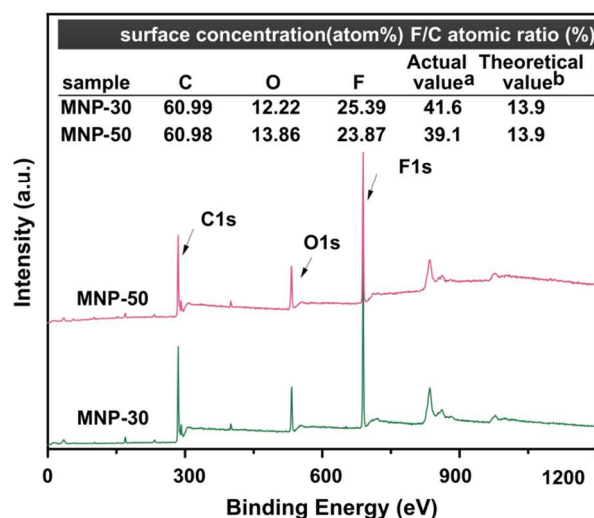


**Fig.4** XPS spectra of MNP-30 and MNP-50. The inset table shows surface elemental concentrations of the samples. <sup>a</sup> The actual values were determined based on the XPS measurement. <sup>b</sup> The theoretical values were calculated based on the known composition of hybrid coating.

### 3.4 Surface wettability

Table 1. Contact angle (CA), advancing contact angle ( $\theta_a$ ), receding contact angle ( $\theta_r$ ), contact angle hysteresis ( $\theta_h$ ), and sliding angle (SA) of different surfaces achieved by CAM 200 optical contact-angle goniometer at room temperature

| samples | CA(°)   | $\theta_a$ (°) | $\theta_r$ (°) | $\theta_h$ (°) | SA(°) |
|---------|---------|----------------|----------------|----------------|-------|
| A       | 110±3   | 117±3          | 95.5±3         | 21.5±4.5       | N/A   |
| B       | 117±3   | 119±2          | 103.1±3        | 16.3±2.8       | N/A   |
| C       | 152±2   | 156±0.2        | 150.2±1.0      | 5.8±1.5        | 4±1.0 |
| D       | 160±0.3 | 160.5±0.2      | 159.5±0.5      | 1.0±0.6        | 1±0.2 |

Sample A, B, C, and D represent the surface of MNP-0, MNP-10, MNP-30, and MNP-50, respectively. N/A: No angles were recorded. The droplet did not roll off even at a 90° tilting angle (ESI Fig. s3 †).

The wetting behavior of the hybrid coating was investigated by the static contact angle (CA) and dynamic contact angle ( $\theta_a$ ,  $\theta_r$ ,  $\theta_h$ ) measurements. CA showed the hydrophobicity of the surface.  $\theta_h$ , calculated from  $\theta_h = \theta_a - \theta_r$ , was related with the force to detach a water droplet from the surface.<sup>24</sup> A lower  $\theta_h$  value revealed that the water can move from the surface more easily. As seen in Table 1, MNP-0 coating with smooth surface had a typical hydrophobic property with relative low CA (110±3°) and a high  $\theta_h$  (21.5±4.5°). On the hybrid coating surfaces, CA increased obviously from 117±3° to 160±0.3°, and  $\theta_h$  reduced from 16.3±2.8° to 1.0±0.6°, with the increasing of MNP@NH<sub>2</sub> contents from 10 wt% to 50 wt%. Compared with the pure copolymer surfaces, MNP-30 and MNP-50 samples

exhibited superhydrophobicity with high CA ( $>150^\circ$ ), low  $\theta_h$  ( $<6^\circ$ ), and ultra low SA ( $<4^\circ$ ), for the fluorinated polymers owned excellent water and oil resisting ability. In case of superhydrophobic surfaces MNP-30 and MNP-50,  $\theta_h$  and SA reduced significantly. This was related with the surface roughness structure and chemical compositions. It indicates that the micro/nanostructure plays a distinct role in maintaining surface superhydrophobicity.

### 3.5 Magnetic property and magnetothermal effect

The magnetic property of hybrid coatings in the dried-state was examined and compared with that of MNP@NH<sub>2</sub>. The magnetization curves show the common S-shape with a very narrow hysteresis in Fig. 5. The magnetization saturation values of these four samples were 56.5, 31.0, 13.0, and 6.68 emu/g, respectively. The saturation magnetizations increased with the rising MNP@NH<sub>2</sub> loadings in the hybrid coatings. It suggests that the copolymer functionalized magnetic particles can be easily manipulated in magnetic field, which is advantageous to their applications.

In addition, in an alternating magnetic field, the hybrid coatings containing Fe<sub>3</sub>O<sub>4</sub> provided a high magnetic heating capability. Typical equipment suitable for the exploration of a magnetically induced coated surface is shown in Fig. 6a. Fig. 6b shows the alternating magnetic field induced heating capability of the covalent integration of MNPs. For MNP-0, no heating effect generated as no temperature change was observed, while for the film with different contents of MNP@NH<sub>2</sub>, various levels of temperature rise had been observed. The temperature of MNP-50 increased from 24 to 44 °C in 25 s under the experimental conditions. This demonstrated that the incorporation of magnetic Fe<sub>3</sub>O<sub>4</sub> brought obvious magnetic field-induced heating property to the hybrid film. It is noteworthy that the high magnetic heating capability of the hybrid films endowed the superhydrophobic surface new function for melting ice without damaging the surface structure.

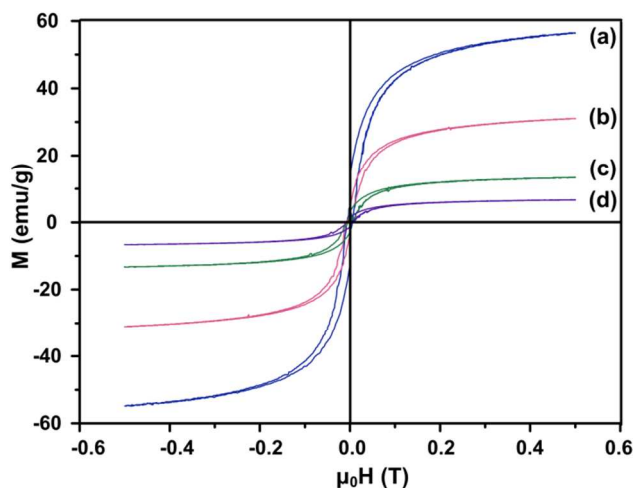
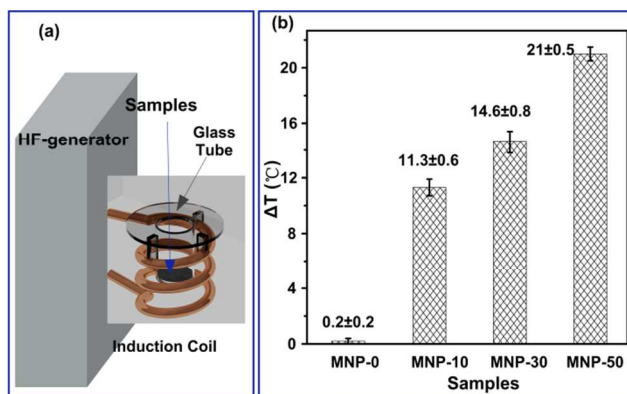


Fig.5 Hysteresis curves of MNP@NH<sub>2</sub> (a), MNP-50 (b), MNP-30 (c), and MNP-10 (d).



**Fig.6** (a) Magnetothermal experimental setup for inductively triggering heating in an alternating magnetic field consisting of a high-frequency generator, a water cooled coil with seven loops having a diameter of 2.5 cm. (b) The heating effect of MNP-0, MNP-10, MNP-30, and MNP-50 surfaces under an alternative magnetic field for 25 s (7.8 KW).

### 3.6 Anti-icing properties

The excellent anti-icing properties of the surface are mainly represented in easily removal of condensed water and crystallization delay of water droplets. The superhydrophobic property of the hybrid coatings with high water contact angle and low hysteresis angle had been confirmed. To further examine the water-adhesion on different superhydrophobic surfaces,<sup>49</sup> we applied an 8  $\mu$ L droplet as probe (Fig. 7) on MNP-10, MNP-30, and MNP-50 surface. For MNP-10 (Fig. 7a<sub>1</sub>-a<sub>4</sub>), as water droplet contacted the coating film, it was inclined to stick on the surface. However, for MNP-30 and MNP-50, water droplets would be lifted from the surface as the needle moved up, which is due to the low water-adhesion. Meanwhile, the water droplet can be stretched long by the weak water-adhesion force. As shown in Fig. 7b<sub>3</sub>, an obvious stretch of water droplet was observed when it was preloaded and then lifted from the surface of MNP-30. In contrast, little deformation of water droplet was observed on MNP-50 surface (Fig. 7c<sub>3</sub>), indicating that the water-adhesion force of MNP-50 surface was lower than that of MNP-30. The roll-off behavior of water droplet was investigated by a high speed camera.<sup>50</sup> As shown in Fig. 7d, when a droplet was dropped on MNP-50 surface, it rolled off quickly within 0.21 s due to the low adhesion force. This indicated that superhydrophobic surface with extremely low water-adhesive force could contribute to timely removal of impacting water droplets (ESI Movie s1†). It would be difficult for droplets to condense on the coating, therefore they can be effectively removed prior to freezing.

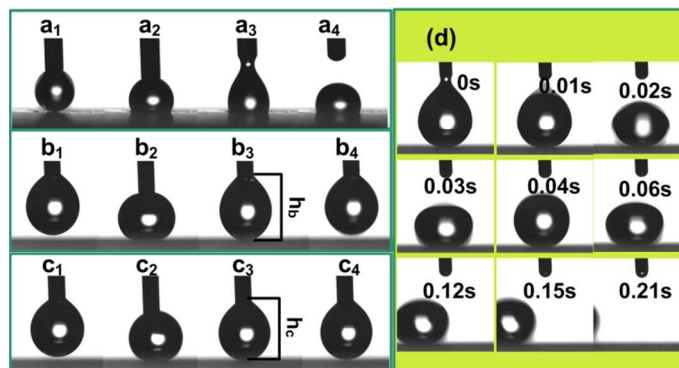


**Fig. 7** Dynamic water-adhesion measurement on surface of MNP-10 ( $a_1$ - $a_4$ ), MNP-30 ( $b_1$ - $b_4$ ), and MNP-50 ( $c_1$ - $c_4$ ), the stretch of water droplet of MNP-30 and MNP-50 were  $h_b$  and  $h_c$ , respectively (obviously  $h_b > h_c$ ). (d) a water droplet roll-off the MNP-50 surface with extremely low adhesive force. The time sequence was shown in the images. When a water droplet was placed on the low adhesive superhydrophobic surface, it rolled off quickly due to the low adhesion force.

Water droplets on the superhydrophobic surface have less intimate contact area with the solid surface because of the vapor pockets existing at the solid-water interface. This heat-insulating effect delays the freezing time of condensed water on the surface under supercooled conditions. In this section, the delay time of the crystallization for condensed water on the different hybrid coatings were tested. The humidity and temperature of environment were controlled to be  $45 \pm 5\%$  and  $-15\text{ }^\circ\text{C}$ , respectively. The photographs of individual water droplets on the hybrid coatings during the whole freezing process are shown in Fig. 8. These droplets were all transparent at first and gradually became opaque after they froze. The delay time (DT) was defined as the time that the water droplet changed from transparent to opaque (frozen). The recorded data demonstrated that the smooth coating of MNP-0 prolonged DT by 1080 s, planar coating of MNP-10 by 1157 s, rough coating of MNP-30 by 2075 s, and superhydrophobic coating of MNP-50 by 2828 s. This indicated that such hybrid superhydrophobic coating prevented ice formation thoroughly, due to the reduced thermal conduction on the superhydrophobic surface and high energy barrier of nucleation for water droplets.<sup>13</sup> Therefore, the low water-adhesive superhydrophobic surface could delay ice formation.

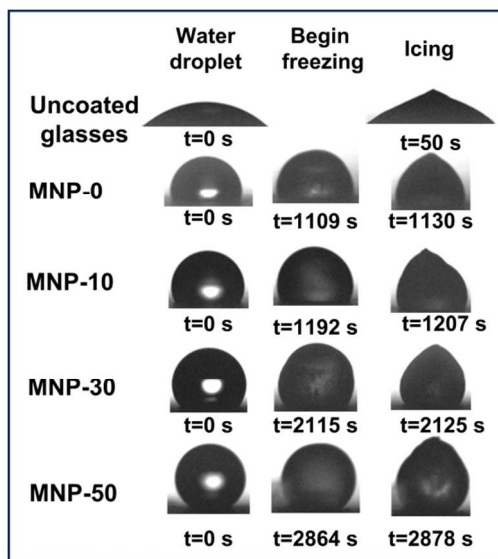


**Fig. 8** Photographs of individual water droplets on glasses with different coatings during the whole freezing process captured by a high speed CCD camera of CAM200 optical contact-angle goniometer.

Although the hybrid superhydrophobic surfaces have a strong ice delay performance, the ice growth still occurs after a certain amount of freezing time at subzero environment. To systematically evaluate the anti-icing potential, we test the ice adhesion strength at  $-5\text{ }^{\circ}\text{C}$  via a self-made measurement device. The ice adhesion strength of four surfaces is shown in Fig. 9. The ice adhesion on the MNP-0 surface was the highest,  $413.7 \pm 17.2$  KPa. For MNP-10, MNP-30, and MNP-50, the ice adhesion strength were  $399.9 \pm 13.8$  KPa,  $296.5 \pm 20.7$  KPa, and  $213.7 \pm 6.9$  KPa, respectively. This could be explained by considering that the superhydrophobic surfaces have low WCA hysteresis and low contact area, driven from the nanostructures on the microspheres.<sup>24,51</sup> Therefore, the multi-scale structures play a large role in ice-phobic.

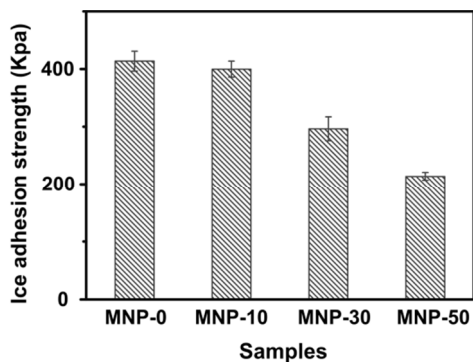


**Fig. 9** Average ice adhesion strengths on four different samples.

### 3.7 Photothermal deicing properties

Beside the magnetically induced heating capability, the hybrid coatings have photothermal stimulus response. The photothermal experimental setup for absorbing light energy from the sunlamp is illustrated in Fig. 10a. Compared with other conventional heating sources, sunlamp features a higher demanding character for the activation of the hybrid coating. Fig. 10b shows the temperature changes of the hybrid coatings under the sunlamp irradiation at ambient temperature. For MNP-0 without magnetic particles, a limited temperature increment was detected in 5 min, from 25 to 27 °C. But for the hybrid coatings of MNP-10, MNP-30, and MNP-50, the surface temperature increase became much higher during the same period. The temperature of MNP-50 increased obviously and exceeded 10 °C after only 1 min of irradiation. The curves show that the surface temperature finally reached an equilibrium value with the surrounding temperature. These results indicate that magnetic particles can give hybrid coatings remarkable photothermal deicing property, which accelerates the ice melting process and shorten the melting time.

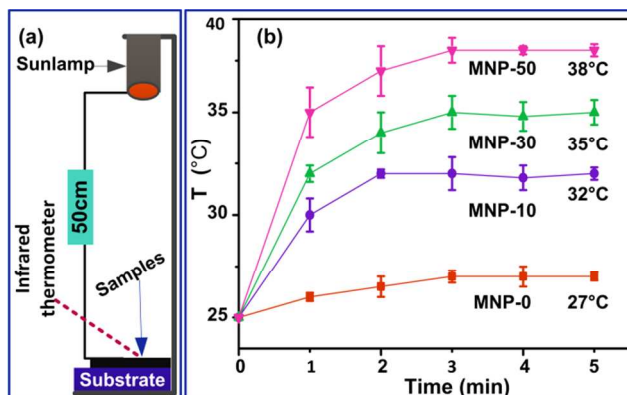


**Fig.10** (a) Photothermal experimental setup for absorbing light energy from sunlamp (used as the solar simulator source), the sample temperature was measured by a non-contact infrared thermometer. (b) The heating effect of coated surfaces under sunlamp irradiation (75 W).

The deicing procedure on the hybrid surface via sunlamp irradiation is as follows. The ice layer formed on the hybrid coatings under the mimic freezing rains. Then the coatings with ice accretion were placed under the sunlamp irradiation at freezing environment below -5 °C. The ice layer and corresponding melting process on the coating surfaces is shown in Fig.11a. As we can see from the Fig.11a<sub>1</sub>-a<sub>4</sub>, the ice accumulated on the whole surface of all the samples. The ice accretion of MNP-0 melted from the top of ice layer (Fig.11a<sub>5</sub>). In contrary, for the coatings with magnetic particles ice melted from the bottom (Fig.11a<sub>6</sub>). The melting time of the ice for the different samples was shown in Fig.11b. The time for ice melting on MNP-0 surface was  $536 \pm 12$  s. In contrast, the melting time for MNP-10, MNP-30, and MNP-50 were  $418 \pm 10$  s,  $306 \pm 6$  s, and  $232 \pm 8$  s, respectively. This indicated that the magnetic particles were the mediators to absorb light energy from the sunlamp. Thus, the magnetic particles in hybrid coatings would be great help to convert optical energy into thermal

energy, and impart the film with thermogenesis deicing function.

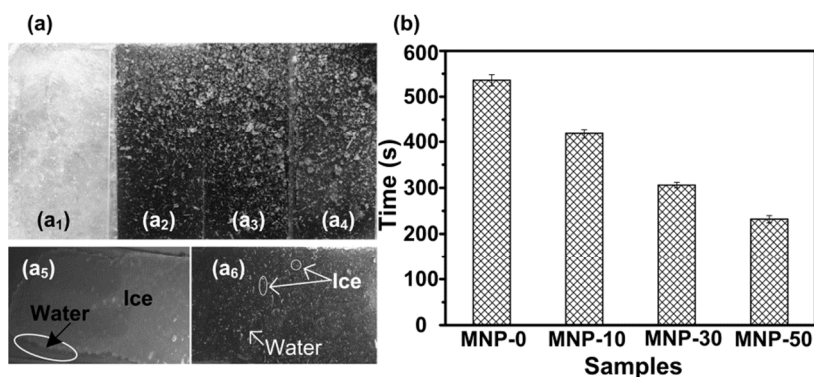


**Fig.11** Pictures (a<sub>1</sub>-a<sub>4</sub>) show the ice layer on surfaces of MNP-0, MNP-10, MNP-30, and MNP-50, respectively. And picture (a<sub>5</sub>) shows the ice on the MNP-0 surface melted from the top of the ice layer, picture (a<sub>6</sub>) shows the ice on the MNP-30 surface melted from the bottom of the ice layer (MNP-10 and MNP-50 were same as that of MNP-30). (b) The time for ice layer to melt under sunlamp.

The influence of repeated icing/deicing process by sunlamp irradiation on the superhydrophobic hybrid coatings was also investigated, as it is more important for practical applications. As shown in Fig. 12, the contact angle of MNP-0, MNP-10, and MNP-30 samples decreased with the increasing number of icing/deicing cycles. While the contact angles of MNP-50 sample were between 159° and 161°, almost kept unchanged during the icing/deicing cycles, which exhibits excellent superhydrophobic maintenance of the coating. That meant the surface roughness structure was not damaged after several icing/deicing cycles. In addition, water droplet was traveling along the arrow on the MNP-50 surface after 10 cycles of icing/deicing, as shown in Fig. 12e and ESI Movie s2 †. After icing/deicing process, its superhydrophobicity was kept on the whole area instead of merely on some points (contact angle measuring points). The outstanding stability of the hybrid coatings could be attributed to the good mechanical property of the epoxy resin and non-contact deicing technology.

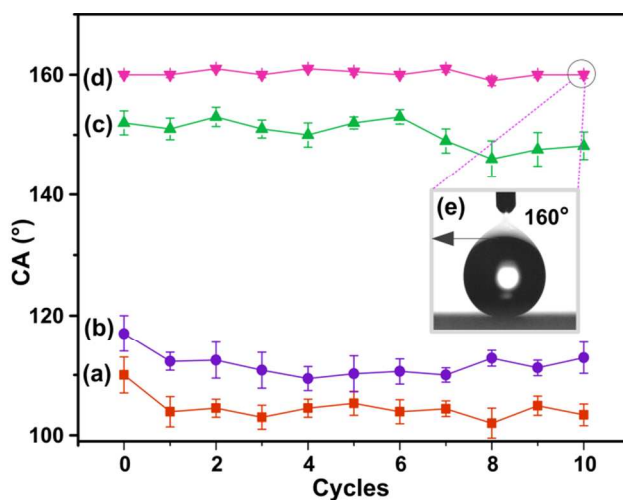
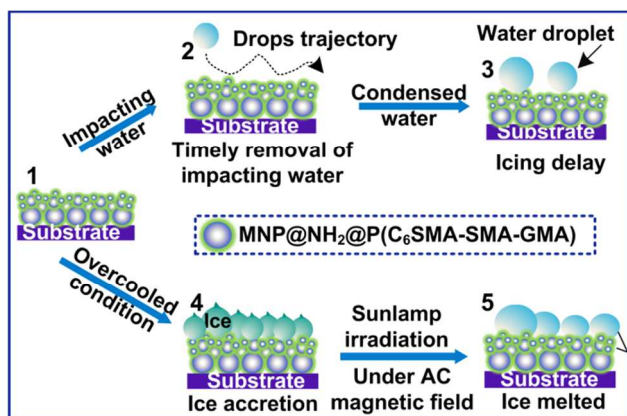


**Fig. 12** Contact angles of MNP-0 (a), MNP-10 (b), MNP-30 (c), and MNP-50 (d) in 10 icing/deicing cycles, (e) Water droplet traveling test after 10<sup>th</sup> icing/deicing cycle of MNP-50.

As a result, the prepared multifunctional hybrid coatings exhibited excellent anti-icing property and active deicing potential. The physical models of anti-icing and deicing processes are shown in Scheme 2. When the condensed water droplets strike the hybrid surface, they easily roll off these superhydrophobic surfaces before freezing, thereby the dynamic freezing process of droplets would be prevented (subgraph 1 and 2). Furthermore, the icing process of condensed water could like to be delayed on the superhydrophobic surface due to the designed micro-nanostructure and introduction of fluorinated groups with low surface energy. Before they freeze, the condensed water droplets could be removed from the substrates via outside powers, including gravity, wind power, and centrifugal forces (subgraph 3). When the coated surfaces are exposed to extremely overcooled environments, ice would accumulate on the hybrid coatings (subgraph 4). With the help of sunlight irradiation or induced heating in the alternating magnetic field, the frost or ice would be melted quickly (subgraph 5). The surfaces could recover and maintain their superhydrophobicity after several cycles. Therefore, the hybrid coatings containing magnetic particles possess excellent anti-icing/deicing performance and show great prospect in anti-icing materials.



Scheme 2. Illustration of anti-icing and deicing properties on superhydrophobic surface.

#### 4. Conclusions

In this work, we reported the fabrication of fluorinated magnetite nanocomposite with the covalent integration, possessing micro-nano roughness structure and stable superhydrophobic properties. The designed novel nanocomposite coating exhibited excellent superhydrophobicity, photothermy, magnetothermal effect, and wetting stability, owing to the tight binding of the nanoparticles on the fluorinated copolymers. The nanocomposite coating with high  $\text{MNP@NH}_2$  contents exhibited special anti-icing property under freezing temperature. The anti-icing/deicing capability and the superhydrophobicity of the coating surface can be enhanced by optimizing the mass content of  $\text{MNP@NH}_2$ . In low temperature ( $-15\text{ }^\circ\text{C}$ , RH  $50 \pm 5\%$ ) condition, the superhydrophobic surfaces can prolong the freezing time from 50 s to 2878 s. Furthermore, the superhydrophobic coatings could reduce the ice adhesion strength greatly. When the coating was in the alternating magnetic field or

under sunlamp irradiation, significant increase of the surface temperature could be detected, which endowed the coating convenient thermal deicing performance. This study offers an effective strategy for fabricating magnetic superhydrophobic surface with excellent anti-icing property and active deicing potential in practical applications.

#### **Acknowledgments**

The authors would like to gratefully acknowledge the National Natural Science Foundation of China (NSFC) for Award No. 21276224, 21476195, 21576236 and Zhejiang Provincial Natural Science Foundation of China for Award No.Y14B060038 for supporting this research.

## References:

- 1 P. Zhang, S. Wang, S. Wang, L. Jiang, *Small*, 2015, **11**, 1939.
- 2 T. Darmanin, F. Guittard, *J. Mater. Chem. A*, 2014, **2**, 16319.
- 3 V. A. Ganesh, H. K. Raut, A. S. Nair, S. Ramakrishna, *J. Mater. Chem.*, 2011, **21**, 16304.
- 4 K. Liu, L. Jiang, *Annu. Rev. Mater. Res.*, 2012, **42**, 231.
- 5 X. Zhang, F. Shi, J. Niu, Y. Jiang, Z. Wang, *J. Mater. Chem.*, 2008, **18**, 621.
- 6 J. Genzer, K. Efimenko, *Biofouling*, 2006, **22**, 339.
- 7 J. Y. Huang, S. H. Li, M. Z. Ge, L. N. Wang, T. L. Xing, G. Q. Chen, X. F. Liu, S. S. Al-Deyab, K. Q. Zhang, T. Chen, Y. K. Lai, *J. Mater. Chem. A*, 2015, **3**, 2825.
- 8 M. Wen, L. Wang, M. Zhang, L. Jiang, Y. Zheng, *ACS Appl. Mater. Interfaces*, 2014, **6**, 3963.
- 9 P. Ragesh, V. A. Ganesh, S. V. Naira, A. S. Nair, *J. Mater. Chem. A*, 2014, **2**, 14773.
- 10 G. D. Bixler, B. Bhushan, *Nanoscale*, 2013, **5**, 7685.
- 11 Y. Wang, J. Xue, Q. Wang, Q. Chen, J. Ding, *ACS Appl. Mater. Interfaces*, 2013, **5**, 3370.
- 12 F. Liu, F. Sun, Q. Pan, *J. Mater. Chem. A*, 2014, **2**, 11365.
- 13 M. Lee, C. Yim, S. Jeon, *J. Chem. Phys.*, 2015, **142**, 41102.
- 14 T. M. Schutzius, S. Jung, T. Maitra, P. Eberle, C. Antonini, C. Stamatopoulos, D. Poulikakos, *Langmuir*, 2015, **31**, 4807.
- 15 L. Wang, M. Wen, M. Zhang, L. Jiang, Y. Zheng, *J. Mater. Chem. A*, 2014, **2**, 3312.
- 16 T. Maitra, M. K. Tiwari, C. Antonini, P. Schoch, S. Jung, P. Eberle, D. Poulikakos, *Nano Lett.*, 2014, **14**, 172.
- 17 X. Zhan, Y. Yan, Q. Zhang, F. Chen, *J. Mater. Chem. A*, 2014, **2**, 9390.
- 18 Y. Tang, Q. Zhang, X. Zhan, F. Chen, *Soft Matter*, 2015, **11**, 4540.
- 19 J. Lv, Y. Song, L. Jiang, J. Wang, *ACS Nano*, 2014, **8**, 3152.
- 20 N. Puretskiy, J. Chanda, G. Stoychev, A. Synytska, L. Ionov, *Adv. Mater. Interfaces*, 2015, DOI: 10.1002/admi.201500124.
- 21 Q. Zhang, M. He, J. Chen, J. Wang, Y. Song, L. Jiang, *Chem. Commun.*, 2013, **49**, 4516.
- 22 A. Davis, Y. H. Yeong, A. Steele, I. S. Bayer, E. Loth, *ACS Appl. Mater. Interfaces*, 2014, **6**, 9272.
- 23 A. J. Meuler, J. D. Smith, K. K. Varanasi, J. M. Mabry, G. H. McKinley, R. E. Cohen, *ACS Appl. Mater. Interfaces*, 2010, **2**, 3100.
- 24 M. Nosonovsky, V. Hejazi, *ACS Nano*, 2012, **6**, 8488.
- 25 M. He, H. Li, J. Wang, Y. Song, *Appl. Phys. Lett.*, 2011, **98**, 93118.
- 26 S. A. Kulinich, M. Farzaneh, *Cold Reg. Sci. Technol.*, 2011, **65**, 60.
- 27 K. K. Varanasi, T. Deng, J. D. Smith, M. Hsu, N. Bhate, *Appl. Phys. Lett.*, 2010, **97**, 234102.
- 28 A. Kim, C. Lee, H. Kim, J. Kim, *ACS Appl. Mater. Interfaces*, 2015, **7**, 7206.
- 29 S. A. Kulinich, M. Honda, A. L. Zhu, A. G. Rozhin, X. W. Du, *Soft Matter*, 2015, **11**, 856.
- 30 S. A. Kulinich, S. Farhadi, K. Nose, X. W. Du, *Langmuir*, 2011, **27**, 25.
- 31 J. Lv, Y. Song, L. Jiang, J. Wang, *ACS Nano*, 2014, **8**, 3152.
- 32 M. Farzaneh, C. C. Ryerson, *Cold Reg. Sci. Technol.*, 2011, **65**, 1.
- 33 N. Dalili, A. Edrisy, R. Carriveau, *Renewable Sustainable Energy Rev.*, 2009, **13**, 428.
- 34 R. G. J. Strens, B. J. Wood, *Mineral. Mag.*, 1979, **43**, 347.

- 35 J. Tang, M. Myers, K. A. Bosnick, L. E. Brus, *J. Phys. Chem. B*, 2003, **107**, 7501.
- 36 M. Y. Razaq, M. Behl, A. Lendlein, *Nanoscale*, 2012, **4**, 6181.
- 37 C. Hsu, C. Wu, Y. Liu, *J. Membr. Sci.*, 2014, **450**, 257.
- 38 A. Hervaultab, N. T. K. Thanh, *Nanoscale*, 2014, **6**, 11553.
- 39 P. Calcagnile, D. Fragouli, I. S. Bayer, G. C. Anyfantis, L. Martiradonna, P. D. Cozzoli, R. Cingolani, A. Athanassiou, *ACS Nano*, 2012, **6**, 5413.
- 40 Y. Xu, J. Yuan, B. Fang, M. Drechsler, M. Müllner, S. Bolisetty, M. Ballauff, A. H. E. Müller, *Adv. Funct. Mater.*, 2010, **20**, 4182.
- 41 L. Zhang, J. Wu, Y. Wang, Y. Long, N. Zhao, J. Xu, *J. Am. Chem. Soc.*, 2012, **134**, 9879.
- 42 J. Fang, H. Wang, Y. Xue, X. Wang, T. Lin, *ACS Appl. Mater. Interfaces*, 2010, **2**, 1449.
- 43 L. Mishchenko, B. Hatton, V. Bahadur, J. A. Taylor, T. Krupenkin, J. Aizenberg, *ACS Nano*, 2010, **4**, 7699.
- 44 Q. Wang, Q. Zhang, X. Zhan, F. Chen, *J. Polym. Sci., Part a: Polym. Chem.*, 2010, **48**, 2584.
- 45 R. Y. Hong, J. H. Li, H. Z. Li, J. Ding, Y. Zheng, D. G. Wei, *J. Magn. Magn. Mater.*, 2008, **320**, 1605.
- 46 L. Xu, M. Kim, K. Kim, Y. Choa, H. Kim, *Colloids Surf., A*, 2009, **350**, 8.
- 47 J. Chen, J. Liu, M. He, K. Li, D. Cui, Q. Zhang, X. Zeng, Y. Zhang, J. Wang, Y. Song, *Appl. Phys. Lett.*, 2012, **101**, 111603.
- 48 B. Feng, R. Y. Hong, L. S. Wang, L. Guo, H. Z. Li, J. Ding, Y. Zheng, D. G. Wei, *Colloids Surf., A*, 2008, **328**, 52.
- 49 Y. Huang, H. Li, L. Wang, Y. Qiao, C. Tang, C. Jung, Y. Yoon, S. Li, M. Yu, *Adv. Mater. Interfaces*, 2015, **2**, DOI: 10.1002/admi.201400433.
- 50 Z. Hu, X. Zhang, Z. Liu, K. Huo, P. K. Chu, J. Zhai, L. Jiang, *Adv. Funct. Mater.*, 2014, **24**, 6381.
- 51 H. Sojoudi, G. H. McKinley, K. K. Gleason, *Mater. Horiz.*, 2015, **2**, 91.

## Graphical abstract

The multifunctional superhydrophobic surfaces incorporated with  $\text{Fe}_3\text{O}_4$  perform excellent anti-icing and active deicing properties.

